Resonant transmission and beaming of cold atoms assisted by surface matter waves

A. I. Fernández-Domínguez,[1] D. Martín-Cano,[1] E. Moreno,[1] L. Martín-Moreno,[2] and F. J. García-Vidal[1]
[1]*Departamento de Física Teórica de la Materia Condensada, Universidad Autónoma de Madrid, E-28049 Madrid, Spain*
[2]*Departamento de Física de la Materia Condensada-ICMA, Universidad de Zaragoza-CSIC, E-50009 Zaragoza, Spain*
(Received 25 April 2008; published 8 August 2008)

We study in detail the appearance of the phenomenon of resonant transmission of matter waves (cold noninteracting atoms) through subwavelength apertures. We show how the emergence of this effect, first reported for electromagnetic waves, is associated with the excitation of surface matter waves, the analog of surface plasmon polaritons in the electromagnetic case. We describe the similarities and differences for the one-dimensional (array of slits) and two-dimensional (array of holes) cases. In this last structure, extraordinary transmission of matter waves is theoretically predicted. Finally, we also study the existence of the beaming effect for matter waves in single apertures flanked by periodic corrugations.

DOI: 10.1103/PhysRevA.78.023614 PACS number(s): 03.75.Be, 37.10.Vz, 73.20.Mf

I. INTRODUCTION

Since the discovery by Ebbesen and co-workers [1] of extraordinary optical transmission (EOT) through two-dimensional (2D) periodic arrays of holes, many theoretical and experimental works have been devoted to the analysis of the transmission properties of perforated metallic films. In addition to EOT in 2D periodic hole arrays [2–6], enhanced transmission has been reported in several other structures: One-dimensional (1D) periodic slit arrays [7–13], 1D periodic hole chains [14], 2D quasiperiodic hole arrays [15–17], and single apertures [18–20]. For the mentioned isolated apertures, it has been also demonstrated that it is possible to tailor the flow of the electromagnetic (EM) fields transmitted through the film by corrugating its output side, thus creating a highly collimated light beam emerging from the aperture [21,22].

From a fundamental point of view, it is now widely accepted that surface EM modes play a key role in the appearance of EOT phenomena. These surface waves transfer light efficiently from the input side of the structure to the output region. For metals in the optical regime, these EM modes are surface plasmon polaritons (SPPs) [23], which require finite negative values of the metal electric permittivity to exist. In the case of perfectly conducting films, which do not support SPPs, the surface texturing plays an active role in creating the corresponding EM modes, as explained in Refs. [24,25].

In the last years, several papers have been presented analyzing the transfer of EOT and beaming phenomena to other undulatory entities such as cold atoms (matter waves) [26,27] or sound (acoustic waves) [28–30]. These reports demonstrate that enhanced transmission and beaming are very general wave processes based on the excitation of surface waves on perforated films. Recently, other electromagnetic phenomena such as optical cloaking [31–33] have been also exported to matter [34] and acoustical [35] waves.

In this paper we describe in detail the existence of EOT and beaming phenomena for noninteracting cold atoms in various geometries. We will show how the resonant excitation of surface matter waves (SMWs) on both sides of a perforated impenetrable film allows the appearance of efficient transmission channels that assist cold atoms to pass through apertures much smaller than their de Broglie wavelength (λ_{dB}). As a difference with SPPs, which propagate on bare vacuum-metal interfaces, SMWs require an attractive potential close to a solid surface in order to be supported. We will focus on a very simple model of SMWs based on square wells which nevertheless contains all physical mechanisms that are behind the resonant transmission and beaming phenomena.

The issue of a feasible experimental implementation of these ideas is worth addressing here. In Ref. [26], we presented a possible experimental scenario for the 1D case (array of slits). The realistic attractive potential supporting SMWs at temperatures around 1 μK (corresponding to a kinetic energy of 10^{-11} eV) could be realized by combining the intrinsic van der Waals attractive interaction between a neutral atom and a dielectric surface—whose typical energies are around 10^{-3} eV [36]—and an external repulsive optical potential created by a blue-detuned laser field propagating along an array of dielectric fibers [37,38]. It is possible that a similar scenario could be used for the practical implementation of the 2D structure (array of holes). We do not attempt to present a detailed implementation here, nevertheless the range of the geometrical parameters necessary to observe resonant transmission for the 1D case, as presented in Ref. [26], will serve as a guide for the design of all structures analyzed throughout this paper.

The paper is organized as follows: Section II is dedicated to the design and analysis of SMWs supported by square potential wells. Section III gives a brief overview of the resonant transmission of cold atoms through 1D periodic slit arrays. In Sec. IV we report on the EOT phenomenon in 2D periodic hole arrays. Section V is devoted to beaming effects associated to resonant transmission of matter waves for the case of a single slit flanked by grooves arranged periodically. Finally, general conclusions are presented in Sec. VI.

II. SURFACE MATTER WAVES

SMWs are solutions of the Schrödinger equation confined in the direction normal to a vacuum-solid interface and propagating along it. Unlike Maxwell equations, which admit confined waves at bare metal-dielectric interfaces, the

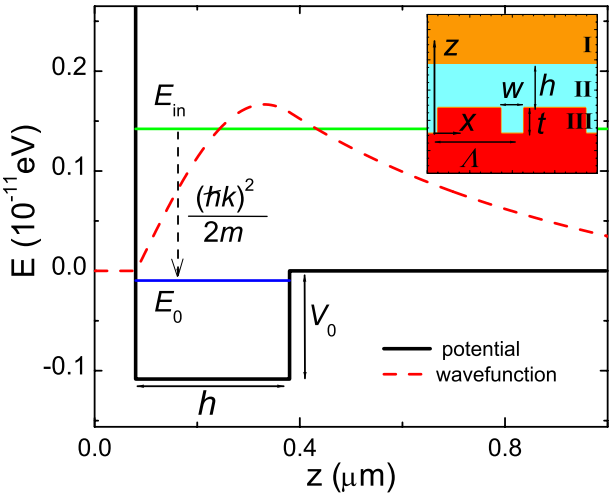

FIG. 1. (Color online) Cross cut along the z direction of the potential function supporting SMWs (black line). The potential well has only one bound state of energy E_0 (blue line). The corresponding wave function (red dashed line) is confined in the z direction. The indicated transition (dashed arrow) from a collision state E_{in} (green line) to the SMWs associated to E_0 is only possible once the surface is modulated. Inset: 2D potential landscape resulting from the corrugation of the material surface. Colors code the potential as follows: Orange (region I): $V=0$; blue (region II): $V=V_0<0$; and red (region III): $V=+\infty$. For the parameters considered in our calculations ($h=0.30$ μm and $V_0=-1.06\times10^{-11}$ eV), $E_0=-0.095\times10^{-11}$ eV.

Schrödinger equation requires an attractive potential close to the material surface for the existence of such waves. The simplest potential supporting SMWs is depicted in Fig. 1 a semi-infinite square well along the z direction (normal to the material surface), translationally invariant in the surface plane. The energies of the bound states ($E_n<0$) associated with this potential well are given by the transcendental equation [39]

$$\tan\left(\sqrt{\frac{2m}{\hbar^2}(E_n-V_0)}h\right)=-\sqrt{\frac{V_0-E_n}{E_n}}, \tag{1}$$

where $V_0<0$ is the potential depth, h its width, and m the mass of the noninteracting atoms forming the SMW.

In what follows, we consider a potential well supporting one single bound state of energy E_0. The dispersion relation of the associated SMWs is

$$E(k)=E_0+\frac{(\hbar k)^2}{2m}, \tag{2}$$

where E and $\hbar k$ are the energy and in-plane momentum of the SMW, respectively. In Fig. 1 a cross cut of the potential function along the z direction is shown. Blue solid line corresponds to the bound state energy E_0, whereas red dashed line renders its wave function. The associated SMWs propagate parallel to the impenetrable surface (modeled by an infinite potential barrier) and decay in the z direction outside the potential well.

Due to energy and momentum conservation principles, SMWs cannot be excited by plane matter waves impinging on the above described structure. It is well known that the periodic corrugation of a flat metallic surface allows the coupling of incident EM radiation with SPPs [23]. The analogous process involving matter waves is shown schematically in Fig. 1: Incident cold atoms of energy E_{in} (green line) are transferred to SMWs after receiving the scattering momentum $\hbar k$ supplied by the structure corrugation. This coupling between plane matter waves and SMWs will later allow the appearance of the resonant transmission phenomenon through perforated films.

With this motivation we calculate the dispersion relation of the SMWs supported by a corrugated structure, namely a groove array of period Λ surrounded by a square potential well of depth $V_0<0$ and thickness h (Fig. 1, inset). The grooves width and depth are w and t, respectively. We develop a quasianalytical formalism based on the modal expansion of the matter wave function (Ψ) within the different regions forming the structure. Taking advantage of the periodic character of the system, we can apply Bloch's theorem and solve Schrödinger equation only inside the unit cell of length Λ. In region I (see inset of Fig. 1), Ψ is written as a sum over diffracted waves as

$$|\Psi_{\text{I}}(z)\rangle=\sum_{n=-\infty}^{\infty}\rho_n|k_n\rangle e^{ik_z^{(n)}z}, \tag{3}$$

where ρ_n are unknown complex coefficients, $k_n=k_x+n\frac{2\pi}{\Lambda}$ and $k_z^{(n)}=\sqrt{k_0^2-k_n^2}$ are the wave-vector components of the Bloch mode $|k_n\rangle$ along x and z directions, respectively. The SMW modal wave vector is k_x, and k_0 is the wave-vector modulus in vacuum $k_0=\sqrt{2mE}/\hbar=2\pi/\lambda_{\text{dB}}$, where E is the SMW energy and λ_{dB} is the de Broglie wavelength. Finally, the wave function in real space for the nth diffracted Bloch mode is $\langle x|k_n\rangle=\frac{e^{ik_nx}}{\sqrt{\Lambda}}$.

In region II, the wave function is expanded again in terms of Bloch modes as

$$|\Psi_{\text{II}}(z)\rangle=\sum_{n=-\infty}^{\infty}(A_ne^{iq_z^{(n)}z}+B_ne^{-iq_z^{(n)}z})|k_n\rangle, \tag{4}$$

where A_n and B_n are the unknown expansion coefficients and $q_z^{(n)}=\sqrt{\xi k_0^2-k_n^2}$, with $\xi=1+\frac{|V_0|}{E}$, is the wave-vector component along the z direction.

In our analysis, we consider groove widths much smaller than λ_{dB} and $\lambda_{\text{dB}}/\sqrt{\xi}$ (the de Broglie wavelength inside the grooves). In this subwavelength regime, taking only the first groove waveguide mode in the expansion of Ψ inside region III results in a very good approximation. This mode governs the SMW behavior as it is the least evanescent wave along the z direction inside the grooves. Thus, in region III we have

$$|\Psi_{\text{III}}(z)\rangle=C\sin(\beta z)|\psi_{\text{WM}}\rangle, \tag{5}$$

where C is unknown. Note that as $\lambda_{\text{dB}}/\sqrt{\xi}\ll w$, the wave vector $\beta=\sqrt{\xi k_0^2-(\pi/w)^2}$ is imaginary and $\sin(\beta z)$ can be replaced by $i\sinh(|\beta|z)$ in Eq. (5). The wave function in real space for the first groove waveguide mode is $\langle x|\psi_{\text{WM}}\rangle=\sqrt{\frac{2}{w}}\sin[\frac{\pi}{w}(x+w/2)]$ inside the groove ($|x|\leqslant w/2$), and

$\langle x|\psi_{WM}\rangle=0$, otherwise. We have chosen $z=0$ at the groove bottom so that $\langle x|\Psi_{III}(0)\rangle=0$.

In order to obtain the set of modal expansion coefficients $\{\rho_n, A_n, B_n, \text{and } C\}$, we impose continuity conditions on Ψ and its z derivative at the interfaces of the system ($z=t$ and $z=t+h$). The wave function and its derivative must be continuous in all space, except at the infinite potential barriers modeling the impenetrable surface, where $\partial_z\Psi$ presents a discontinuity. Thus, in order to remove their dependence on the x coordinate, we project the matching equations at $z=t+h$ onto Bloch modes, whereas equations at $z=t$ associated to Ψ ($\partial_z\Psi$) must be projected onto $|k_n\rangle$ ($|\psi_{WM}\rangle$). Defining the quantity $\psi=C\sin(\beta t)$, which corresponds to the amplitude of Ψ at the openings of the grooves, we obtain a single continuity equation of the form

$$(G-\epsilon)\psi=0. \tag{6}$$

The term $\epsilon=\beta/[k_0\tan(\beta t)]$ contains the effect of the penetration of matter waves inside the grooves. Its physical meaning can be clarified by comparison with the case of wide grooves, where β is a real number, and thus propagating modes are supported inside each groove. In such case the zeros of the denominator in ϵ correspond to resonances within the grooves due to bouncing of the groove mode at the bottom and opening of the indentation. For the chosen subwavelength grooves, β is imaginary and no propagating modes nor resonances exist, but the interpretation of ϵ is analog. The G term reflects the coupling of the matter wave function at different grooves through diffracted waves and is given by

$$G=\sum_{n=-\infty}^{\infty}\frac{iq_z^{(n)}}{k_0}f(k_n,h)|\langle k_n|\psi_{WM}\rangle|^2, \tag{7}$$

where the function $f(k_n,h)$ is

$$f(k_n,h)=\frac{k_z^{(n)}\cos(q_z^{(n)}h)-iq_z^{(n)}\sin(q_z^{(n)}h)}{q_z^{(n)}\cos(q_z^{(n)}h)-ik_z^{(n)}\sin(q_z^{(n)}h)}. \tag{8}$$

For $k_n=0$, the denominator in $f(k_n,h)$ vanishes for energies satisfying Eq. (1). This fact indicates the close link between the bound states supported by the potential well surrounding the modulated surface and resonances in the G term, which governs the coupling between different grooves. The dispersion relation of the SMWs propagating along the structure is obtained by imposing the condition $|G-\epsilon|=0$, leading to nonzero solutions of Eq. (6). This condition can be rewritten as

$$\cot(\beta t)=\sum_{n=-\infty}^{\infty}\frac{iq_z^{(n)}}{\beta}f(k_n,h)|\langle k_n|\psi_{WM}\rangle|^2. \tag{9}$$

In Fig. 2, $|G-\epsilon|$ for an array period of $\Lambda=0.80$ μm is plotted. The groove dimensions are $w=t=0.16$ μm. The attractive potential depth is $V_0=-1.06\times10^{-11}$ eV and its width $h=0.30$ μm. As explained above, this set of parameters is tuned to observe resonant transmission for the 1D case. Black regions correspond to $|G-\epsilon|$ values close to zero, showing the dispersion relation of the SMWs supported by the structure. In our calculations, we have considered that

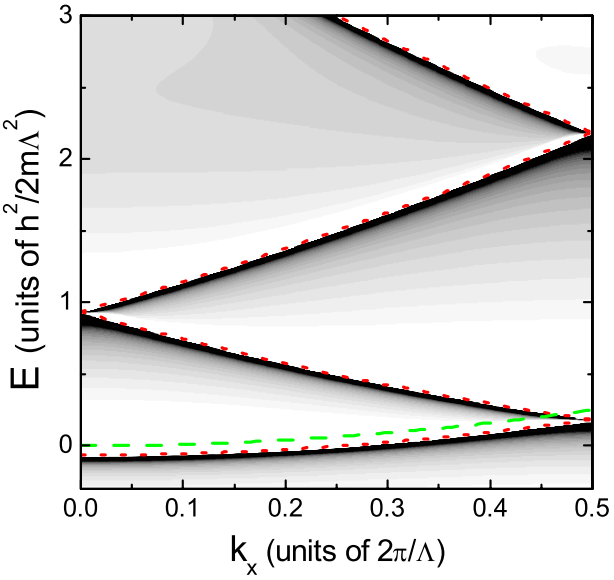

FIG. 2. (Color online) Dispersion relation of the SMWs supported by the groove array depicted in the inset of Fig. 1. The array period is $\Lambda=0.80$ μm and the groove dimensions, $w=t=0.16$ μm. The potential well depth and thickness are $V_0=-1.06\times10^{-11}$ eV and $h=0.30$ μm, respectively. The SMWs are composed by cold ^{87}Rb atoms ($m=1.45\times10^{-25}$ kg). Red dotted lines correspond to the approximated bands obtained from Eq. (2). Green dashed line renders E versus k_x for free ^{87}Rb atoms.

SMWs are composed of cold ^{87}Rb atoms ($m=1.45\times10^{-25}$ kg). Kinetic energy versus momentum for free ^{87}Rb atoms is depicted as the dashed green line. Note that SMWs are strictly guided modes only below this line. The solutions of k_x of Eq. (6) have an additional imaginary part. This means that above this line SMWs are leaky, radiating while they propagate along the structure.

An approximate expression for the dispersion relation of SMWs on corrugated surfaces can be extracted from Eq. (2) by simply applying Bloch's theorem to the parallel momentum component $k=k_x$. This leads to different bands of energy $E_n(k_x)=E_0+(\hbar^2/2m)(k_x+n\frac{2\pi}{\Lambda})^2$ shown as red dotted line in Fig. 2. For the potential well considered in our calculations, $E_0=-0.095\times10^{-11}$ eV is much lower than the kinetic energy close to the $n=1$ band edge, $h^2/2m\Lambda^2=1.48\times10^{-11}$ eV. As we can see in Fig. 2, this approximated expression is in very good agreement with the exact SMWs dispersion relation.

III. RESONANT TRANSMISSION THROUGH 1D SLIT ARRAYS

Once we have designed SMWs with properties similar to those of SPPs, we study the appearance of the extraordinary transmission phenomenon for cold atoms [26]. We go further with our simple model and consider a material slab perforated with a periodic array of narrow slits and surrounded by a square potential well (see right-hand inset of Fig. 3). Such structure supports SMWs at both film sides which, as in the electromagnetic analog, will play a crucial role in the resonant transmission process. The close correspondence be-

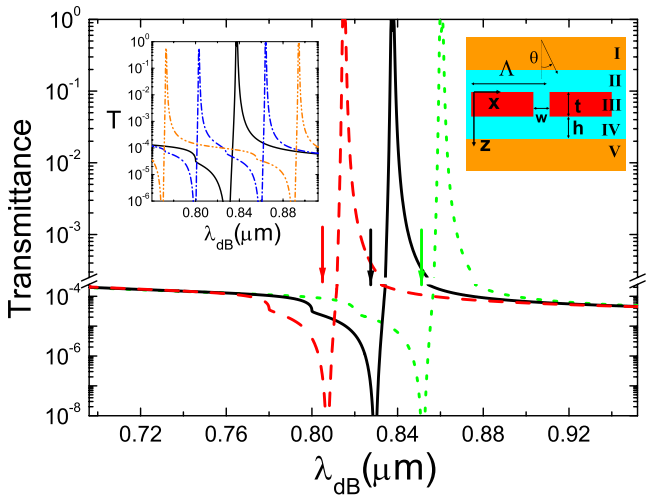

FIG. 3. (Color online) Cold ^{87}Rb atoms transmission spectrum through a film of thickness $t=0.16$ μm perforated with a periodic array of slits of width $w=0.22$ μm. Three different array periods are considered: $\Lambda=0.80$ μm (black solid line); $\Lambda=0.78$ μm (red dashed line); and $\Lambda=0.82$ μm (green dotted line). Vertical arrows indicate the values of $\lambda_{\mathrm{dB}}^{\mathrm{SMW}}$ obtained from Eq. (13) for each case. Left-hand inset renders T versus λ_{dB} for $\Lambda=0.80$ μm and three different incidence angles: $\theta=0°$ (black solid line); $\theta=2°$ (blue dashed-dotted line); and $\theta=4°$ (orange dashed-double-dotted line). Right-hand inset: 2D display of the perforated material film ($h=0.30$ μm and $V_0=-1.06\times10^{-11}$ eV). Regions I, V: $V=0$; II, IV: $V=V_0$; III: $V=+\infty$.

tween the Schrödinger equation and Maxwell equations in two dimensions leads to several similarities between EOT in slit arrays for cold atoms and s-polarized light [40].

We extend the modal expansion formalism presented above to study the transmission of a plane matter wave impinging from the top ($z<0$) on the perforated film. The wave function in region I (see Fig. 3) can be written as an incident plane wave with parallel momentum $k_{\mathrm{inc}}=\sqrt{2mE}/\hbar \sin\theta = 2\pi \sin\theta/\lambda_{\mathrm{dB}}$ (where θ is the incidence angle) plus a sum over reflected propagating and evanescent Bloch modes $|k_n\rangle$, with $k_n=k_{\mathrm{inc}}+n\frac{2\pi}{\Lambda}$. Inside the attractive potential well surrounding the material slab (regions II and IV), Ψ is given by Eq. (4), whereas the transmitted matter wave (region V) can be expanded in terms of diffracted Bloch modes $|k_n\rangle$.

For subwavelength slits ($w \ll \lambda_{\mathrm{dB}}, \lambda_{\mathrm{dB}}/\sqrt{\xi}$) the behavior of the matter waves inside region III is accurately described by considering only the first slit waveguide mode $|\psi_{\mathrm{WM}}\rangle$ in the expansion

$$|\Psi_{\mathrm{III}}(z)\rangle = (Ce^{i\beta z} + De^{-i\beta z})|\psi_{\mathrm{WM}}\rangle. \tag{10}$$

Imposing continuity conditions on the wave function and its z derivative at the structure interfaces, we end up with a set of two linear equations in the amplitudes of the matter wave function at the entrance, $\psi=C+D$, and exit, $\psi'=-(Ce^{i\beta t}+De^{-i\beta t})$, of the slits,

$$(G-\epsilon)\psi - G^V\psi' = I,$$

$$(G-\epsilon)\psi' - G^V\psi = 0. \tag{11}$$

Extending the physical picture that we have associated to Eq. (6), the upper (lower) equation in system (11) controls the matter wave behavior at the input (output) film surface. Thus, the inhomogeneous term $I=(2\sqrt{2}i/\pi)\xi/[\xi\cos(\xi k_0 h) - i\sin(\xi k_0 h)]$ present only in the upper equation, gives the overlap between the incident matter plane wave and the slits waveguide mode $|\psi_{\mathrm{WM}}\rangle$. The term $G^V=\beta/[k_0\sin(\beta t)]$ describes the coupling of Ψ at both sides of the film through the slits, whereas ϵ remains the same as in the previous section. Finally, G, which describes the coupling of the matter wave function at different slits openings, is given by Eq. (7).

Solving Eqs. (11), amplitudes ψ and ψ' are obtained. The matter wave function in each point of the space and also the transmissivity (T) of the structure can be then calculated. Within our formalism, the last one is given by

$$T = \frac{\int_\Lambda j_z^t(x)dx}{\int_\Lambda j_z^i(x)dx} = G^V \mathrm{Im}(\psi^*\psi'), \tag{12}$$

where $j_z^{t(i)}(\mathbf{r})=(\hbar/m)\mathrm{Im}\{\Psi^{t(i)}(\mathbf{r})^*\partial_z\Psi^{t(i)}(\mathbf{r})\}$ is the z component of the probability density current associated to the transmitted (incident) matter waves.

Figure 3 renders, in logarithmic scale, the transmittance of cold ^{87}Rb atoms impinging at normal incidence on a film of thickness $t=0.16$ μm perforated with a periodic array of slits of width $w=0.22$ μm. The potential depth is $V_0=-1.06\times10^{-11}$ eV and its width $h=0.3$ μm. Three different array periods are considered: $\Lambda=0.80$ μm (black solid line); $\Lambda=0.78$ μm (red dashed line); and $\Lambda=0.82$ μm (green dotted line). Spectra are normalized to the current flux impinging on the array period. Close to Λ, all of the structures display a sharp dip in transmittance ($T=0$ within the numerical precision of our calculations) followed by two adjacent narrow 100% transmission peaks. Note that these two peaks cannot be distinguished in Fig. 3 due to the wide spectral region displayed. In the electromagnetic analog, these are the main fingerprints of the presence of EOT [11]. Their appearance in Fig. 3 indicates that the resonant transmission phenomenon for cold atoms occurs in our model structures.

The physical origin of EOT relies on the resonant excitation of SPP modes supported by metallic films [3]. In order to confirm that SMWs are the key actors in the formation of the analogous phenomenon for matter waves, we compare the spectral position of the transmission resonances with the approximate predictions obtained from the dispersion relation of SMWs on uncorrugated interfaces (2). Since the coupling between the incident atom beam and SMWs is mainly governed by first-order processes ($n=\pm1$), at normal incidence the parallel momentum of the SMWs propagating along the film surface is $k_\pm=2\pi/\Lambda$. Thus, the corresponding de Broglie wavelength is

$$\lambda_{\mathrm{dB}}^{\mathrm{SMW}} = \frac{\Lambda}{\sqrt{1+(2mE_0/h^2)\Lambda^2}} \simeq \Lambda\left(1+\frac{2m|E_0|\Lambda^2}{h^2}\right), \tag{13}$$

where we have taken into account that, for the parameters we are considering $|E_0| \ll h^2/2m\Lambda^2$. For the three arrays of Fig.

3, λ_{dB}^{SMW} (indicated by vertical short arrows) coincides with the position of the sharp dip in transmission spectra. In the EOT phenomenon, this close correspondence between the position of the so-called Wood's anomaly and the frequency of the SPPs supported by the uncorrugated metal surface has been also observed [10]. In the preceding section, we showed that the exact SMWs dispersion relation (9) leads to lower energies than predicted from this approximation. This fact, together with the interaction through the slits of the SMWs at both sides of the film shifts the spectral location of the transmission peaks to larger λ_{dB}.

Although the dispersion relation of the SMWs supported by the film predicts the position of the resonant peaks in transmission spectra, it does not contain any information about the peaks shape. In order to understand the asymmetric profile of the transmission maxima in Fig. 3, a more complex interpretation based on a Fano-type picture [41] is required. Such scheme, which has been successfully applied to the analysis of EOT in its electromagnetic version [42], distinguishes between two different contributions to the transmission process: A resonant contribution due to the excitation of surface waves on the film sides and a nonresonant contribution due to the direct scattering of the incident radiation through the apertures. The interference between these two channels induces the observed asymmetry in the transmission maxima. According to this picture, the Wood's anomaly can be associated to the destructive interference between these two channels.

In the left-hand inset of Fig. 3, T versus λ_{dB} for an array of period $\Lambda=0.80$ μm and three different incidence angles (θ) is shown. For non-normal incidence, $\theta=2°$ (blue dashed-dotted line) and $\theta=4°$ (orange dashed-double-dotted line), T displays the characteristic resonant features twice, located at larger and lower λ_{dB} than at normal incidence (black solid line). This splitting of the resonances with the angle of incidence can be understood again in terms of SMWs on uncorrugated interfaces. For $\theta \neq 0$, the incident atom beam excites SMWs with two different parallel momenta $k_{\pm} = 2\pi(\sin\theta/\lambda_{dB} \pm 1/\Lambda)$. This leads to the formation of two very efficient transmission channels with different resonant energies $E(k_x^{\pm})$. For small θ, a simple expression for the λ_{dB} associated to these SMWs can be obtained,

$$\lambda_{dB}^{SMW\pm}(\theta) = \lambda_{dB}^{SMW}\left(1 \pm \frac{\theta}{\sqrt{1+(2mE_0/h^2)\Lambda^2}}\right), \qquad (14)$$

where λ_{dB}^{SMW} is given by Eq. (13). This result is in very good agreement with the spectra depicted in the left-hand inset of Fig. 3. As predicted, for small angles the transmission peaks deviate linearly with θ from the normal incidence position.

IV. RESONANT TRANSMISSION THROUGH 2D HOLE ARRAYS

The next step in our analysis is to transfer the resonant transmission phenomenon from 1D structures (slit arrays) to 2D ones (hole arrays), for which EOT was first reported [1]. As in the 1D case, the 2D SMWs are supported by a square potential well surrounding the material film drilled with the hole arrangement. SMWs propagate along the film surface (xy plane) and decay in the z direction for increasing distances from the film.

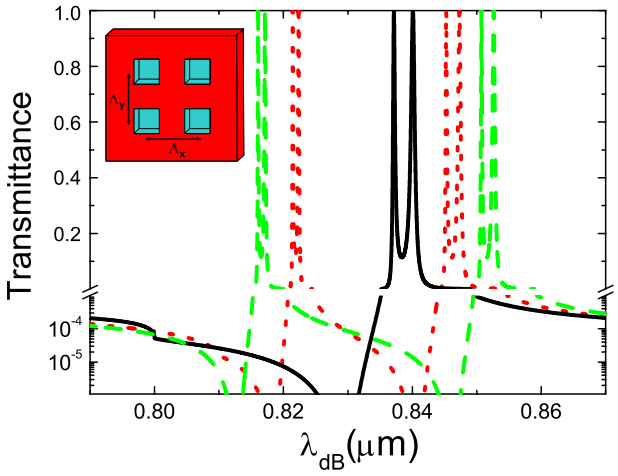

FIG. 4. (Color online) Transmittance of cold ^{87}Rb atoms through a film of thickness $t=0.16$ μm drilled with a periodic array of square holes of side $w=0.28$ μm as a function of λ_{dB}. Three different structures are considered. Black solid line: Square array with $\Lambda_x=\Lambda_y=0.800$ μm. Red dotted line: Rectangular array with $\Lambda_x=0.790$ μm and $\Lambda_y=0.810$ μm. Green dashed line: $\Lambda_x=0.785$ μm and $\Lambda_y=0.815$ μm. Inset: Schematic view of the structure.

We study the scattering of cold atoms by rectangular arrays of holes (see the inset of Fig. 4) by means of an extension of the formalism applied to 1D structures. For 2D periodic arrays, Bloch's theorem labels the parallel momentum associated to the discrete diffraction orders with two indexes (n and m),

$$\mathbf{k}_{nm} = \mathbf{k}_{inc} + n\frac{2\pi}{\Lambda_x}\hat{\mathbf{x}} + m\frac{2\pi}{\Lambda_y}\hat{\mathbf{y}}, \qquad (15)$$

where the incident parallel momentum $\mathbf{k}_{inc} = \sqrt{2mE}/\hbar(\sin\theta\sin\phi\hat{\mathbf{x}} + \sin\theta\cos\phi\hat{\mathbf{y}})$ is characterized by the polar (θ) and azimuthal (ϕ) angles, and Λ_x and Λ_y are the array periods in the x and y directions, respectively. Bloch modes, $|\mathbf{k}_{nm}\rangle$, form the eigenmode basis onto which the matter wave function is expanded outside the film. The associated wave functions in real space are $\langle \mathbf{r}_{\parallel}|\mathbf{k}_{nm}\rangle = e^{i\mathbf{k}_{nm}\mathbf{r}_{\parallel}}/\sqrt{\Lambda_x\Lambda_y}$, where $\mathbf{r}_{\parallel} = x\hat{\mathbf{x}} + y\hat{\mathbf{y}}$.

We focus our analysis on two different aperture shapes: Rectangular holes (characterized by the hole sides w_x and w_y) and circular holes (characterized by the hole radius r_c). In both cases, the hole dimensions are much smaller than the de Broglie wavelength, i.e., $w_x, w_y, r_c \ll \lambda_{dB}/\sqrt{\xi}$. Thus, as for 1D slits, it is a good approximation to consider only the first hole waveguide mode $|\psi_{WM}^{2D}\rangle$ in the description of Ψ inside the slab, having

$$|\Psi_{III}(z)\rangle = (Ce^{i\beta_{2D}z} + De^{-i\beta_{2D}z})|\psi_{WM}^{2D}\rangle, \qquad (16)$$

where, for rectangular holes, the waveguide mode is given by

$$\langle \mathbf{r}_\parallel | \psi_{\mathrm{WM}}^{\mathrm{2D}} \rangle = \langle x | \psi_{\mathrm{WM}} \rangle \langle y | \psi_{\mathrm{WM}} \rangle = \frac{2}{\sqrt{w_x w_y}} \sin\left[\frac{\pi}{w_x}\left(x + \frac{w_x}{2}\right)\right] \sin\left[\frac{\pi}{w_y}\left(y + \frac{w_y}{2}\right)\right] \tag{17}$$

inside the hole and $\langle \mathbf{r}_\parallel | \psi_{\mathrm{WM}}^{\mathrm{2D}} \rangle = 0$, otherwise. The z component of the wave vector is $\beta_{\mathrm{2D}} = \sqrt{\xi k_0^2 - (\pi/w_x)^2 - (\pi/w_y)^2}$.

For circular holes, the wave function for the fundamental waveguide mode inside the hole is

$$\langle \mathbf{r}_\parallel | \psi_{\mathrm{WM}}^{\mathrm{2D}} \rangle = \frac{1}{\sqrt{\pi r_c^2 [J_1(r_{01})]^2}} J_0\left(\frac{r_{01}}{r_c} r\right), \tag{18}$$

where $J_0(r)$ and $J_1(r)$ are the zero and first-order Bessel functions of the first kind, respectively, and $r_{01} \approx 2.4048$ is the first zero of $J_0(r)$. The wave vector along the z direction is $\beta_{\mathrm{2D}} = \sqrt{\xi k_0^2 - (r_{01}/r_c)^2}$. Note that the fundamental waveguide mode of the hole depends only on the radial coordinate $r = \sqrt{x^2 + y^2}$.

The continuity equations obtained from the modal expansion procedure for 2D hole arrays keep the same form as for 1D slit arrays [Eqs. (11)], where now the unknowns, ψ and ψ', are equal, except for a phase factor, to the wave-function amplitudes at the hole openings. The physical interpretation and the definition of the different terms also holds, with the only difference that wave vector β must be replaced by its 2D counterpart β_{2D}. $G = G_{\mathrm{2D}}$ is the only term within Eqs. (11) which varies substantially from its 1D version. It includes now a double sum over diffraction orders,

$$G_{\mathrm{2D}} = \sum_{n,m=-\infty}^{\infty} \frac{i q_z^{(nm)}}{k_0} f(\mathbf{k}_{nm}, h) |\langle \mathbf{k}_{nm} | \psi_{\mathrm{WM}}^{\mathrm{2D}} \rangle|^2, \tag{19}$$

where $f(\mathbf{k}_{nm}, h)$ is given by Eq. (8) substituting $k_z^{(n)}$ and $q_z^{(n)}$ by $k_z^{(nm)} = \sqrt{k_0^2 - |\mathbf{k}_{nm}|^2}$ and $q_z^{(nm)} = \sqrt{\xi k_0^2 - |\mathbf{k}_{nm}|^2}$, respectively. Once the set of matching equations is solved, T can be evaluated from Eq. (12), where now the total probability current fluxes are integrated inside the 2D unit cell of area $\Lambda_x \times \Lambda_y$.

Figure 4 shows the transmittance of cold ^{87}Rb atoms at normal incidence through a material slab ($t = 0.16$ μm). Three different periodic arrays of square holes are considered. In all three cases $w_x = w_y = 0.28$ μm. Black line corresponds to a square array of period $\Lambda_x = \Lambda_y = 0.80$ μm. It shows the characteristic twin maxima accompanied by a sharp dip close to the period already analyzed for 1D structures. In contrast to Fig. 3, in Fig. 4 the two resonant peaks are clearly distinguishable since the wavelength range displayed is much narrower. As in the 1D case, both resonant maxima are linked to the excitation of SMWs at both film surfaces. However, since the coupling of the SMWs through the apertures (both slits and holes) is evanescent (β and β_{2D} are imaginary for the geometrical parameters considered), two different configurations of the matter wave function arises. The two possible profiles of Ψ correspond to the symmetric and antisymmetric superposition of the isolated SMWs through the apertures. It is discussed below how the symmetric (antisymmetric) profile with respect to the middle of the film is higher (lower) in energy, leading to a resonant peak at a shorter (larger) λ_{dB} in the transmission spectrum.

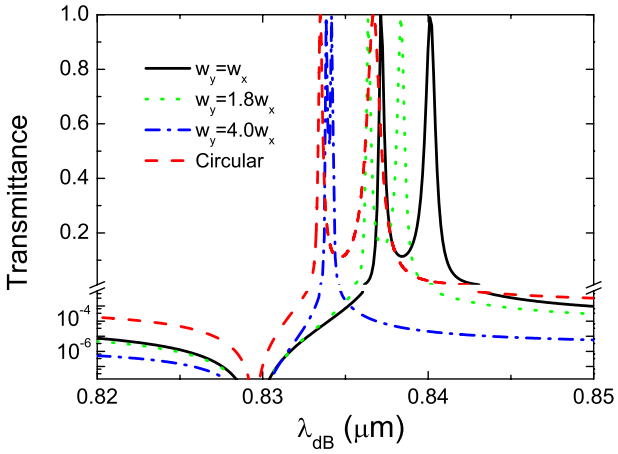

FIG. 5. (Color online) Cold ^{87}Rb atoms transmission through square arrays ($\Lambda_x = \Lambda_y = 0.800$ μm) of holes of area equal to 7.84×10^{-2} μm^2. Four different hole shapes are considered (see main text). The rest of the parameters defining the structure are the same as in Fig. 4.

The transmittance versus λ_{dB} for two rectangular arrays of periods $\Lambda_x = 0.790$ μm, $\Lambda_y = 0.810$ μm (red dotted line), and $\Lambda_x = 0.785$ μm, $\Lambda_y = 0.815$ μm (green dashed line) is also plotted in Fig. 4. Although both arrays are almost square, the transmission spectra are very different from the square one. Rectangular arrays present the usual resonant features twice. This splitting can be understood again turning back to Eq. (2). In 1D arrays under non-normal incidence, nonzero $\mathbf{k}_{\mathrm{inc}}$ allows the excitation of SMWs with two different wave vectors $\mathbf{k}_\pm$, leading to different resonant energies $E(\mathbf{k}_\pm)$. In 2D rectangular hole arrays, it is the fact that $\Lambda_x \neq \Lambda_y$ what makes the resonant energies associated to SMWs propagating along x and y direction different, i.e., $E(\mathbf{k}_{10}) \neq E(\mathbf{k}_{01})$. As expected, transmission resonances for both rectangular arrays in Fig. 4 are located close to Λ_x and Λ_y. This splitting of transmission resonances in rectangular hole arrays does not occur in the electromagnetic case, where the incident light excites only SPPs traveling along the direction defined by the electric field component parallel to the metallic film. Thus, the polarization of the incident light defines a preferred direction at the film surface and only transmission resonances associated to the structure periodicity along that direction appear in the spectra [14].

In order to study the dependence of the transmission properties of hole arrays on the hole shape, the transmission spectra for square arrays of period $\Lambda_x = \Lambda_y = 0.800$ μm and four different hole geometries are shown in Fig. 5. The geometrical parameters of the perforated film are the same as in Fig. 4. The hole area is fixed to 7.84×10^{-3} μm^2. Black solid line renders the transmittance for square holes of side $w_x = w_y = 0.28$ μm. Green dotted and red dashed-dotted lines correspond to rectangular arrays of side $w_x = 0.21$ μm and $w_y = 0.37$ μm, and $w_x = 0.14$ μm and $w_y = 0.56$ μm, respectively. The transmission spectrum for circular holes of radius $r_c = 0.16$ μm is plotted as red dashed line. The profile of the transmission maxima for the four structures is very similar,

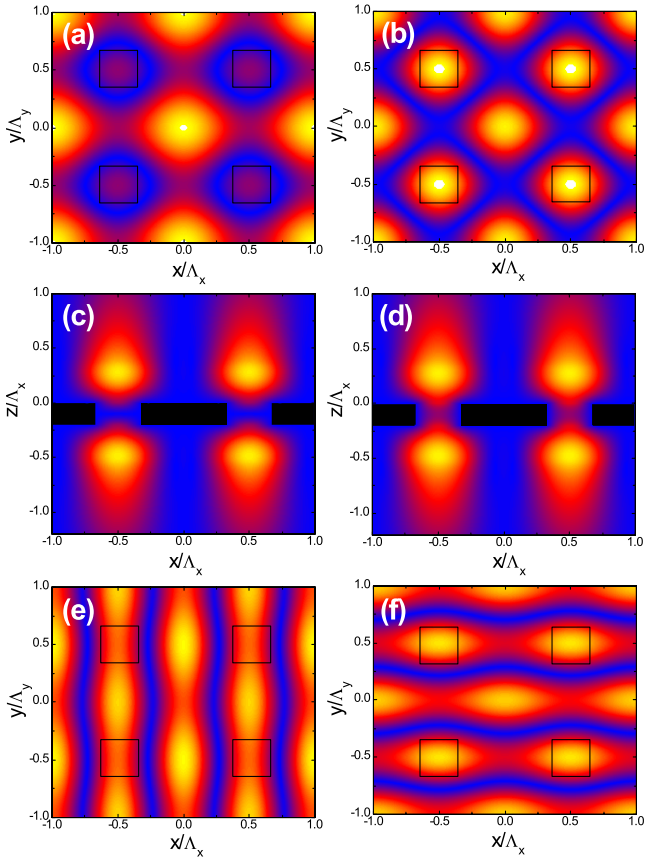

FIG. 6. (Color online) Modulus of the matter wave function passing through periodic hole arrays at resonance. Panels (a) and (b): At the output surface of the square array considered in Fig. 4 for $\lambda_{dB}=0.829\ \mu$m and $\lambda_{dB}=0.837\ \mu$m, respectively. Panels (c) and (d): Cross cut in the xz plane for $\lambda_{dB}=0.837\ \mu$m and $\lambda_{dB}=0.840\ \mu$m. Panels (e) and (f): $|\Psi|$ at the output surface for the rectangular array in green in Fig. 4 evaluated at $\lambda_{dB}=0.816\ \mu$m and $\lambda_{dB}=0.850\ \mu$m. $|\Psi|$ increases from blue (black) to yellow (white). Black squares indicate hole positions.

whereas their width and position change. Thus, although the width of the peaks for square and circular holes is the same, the spectral position is shifted to shorter λ_{dB} in the circular case. This blueshift of the transmission resonances also occurs for rectangular holes, accompanied by a reduction of the peaks width. The ratio between hole sides control this effect: For larger w_y/w_x, the transmission peaks approach the periodicity while they become narrower.

In Fig. 6, the wave-function modulus, $|\Psi|$ passing through the hole arrays of Fig. 4 is depicted. Upper panels show $|\Psi|$ in the output side ($z=0.36\ \mu$m) of the square array of Fig. 4. Panel (a) corresponds to the transmission dip at $\lambda_{dB}=0.829\ \mu$m and panel (b) to the peak at $\lambda_{dB}=0.837\ \mu$m. As expected from Eq. (12), the wave-function modulus at the holes exit presents a minimum (maximum) at the resonant dip (peak) in the spectrum. However, in both cases it displays a maximum in the center of the square formed by four neighbor holes in the array. These maxima do not appear in the electromagnetic case [43] due to the asymmetry of the electric field induced by the incident polarization. Panels (c) and (d) show a cross cut of the matter wave function inside the xz plane for the same structure. They correspond to the resonant transmission peaks at $\lambda_{dB}=0.837\ \mu$m and $\lambda_{dB}=0.840\ \mu$m, respectively. They show clearly that the maximum at higher (lower) λ_{dB} is linked to a symmetric (antisymmetric) profile of Ψ with respect to the middle plane of the perforated film. As a result, the modulus of the wave function inside the holes vanishes at $z=\frac{t}{2}$ in panel (c), whereas $|\Psi|$ presents a minimum different from zero inside the holes in panel (d).

Finally, lower panels in Fig. 6 render the matter wave function at resonance in the output surface of the rectangular hole array in green in Fig. 4. Panel (e) is evaluated at $\lambda_{dB}=0.816\ \mu$m and panel (f) at $\lambda_{dB}=0.850\ \mu$m. These two panels demonstrate that the resonant transmission process for $\lambda_{dB}\simeq\Lambda_x$ is controlled by SMWs propagating along the x direction, whereas for $\lambda_{dB}\simeq\Lambda_y$, SMWs traveling in the y direction assist it.

V. RESONANT TRANSMISSION AND BEAMING THROUGH SINGLE APERTURES

In this section we study the phenomenon of resonant transmission and beaming through single apertures for matter waves. It is well known that SPPs, which are key actors in the electromagnetic version of EOT, also constitute a route to mold the flow of light [21]. SMWs can be tailored in a similar way to SPPs in order to control the diffraction of matter waves exiting from a single aperture [27]. We consider a simple 1D structure composed by a central slit flanked by an array of grooves symmetrically disposed at both sides (right and left) of the aperture in both faces (input and output) of the film.

We extend our theoretical formalism to deal with finite structures. We consider an artificial supercell of length L containing the structure shown in the right-hand inset of Fig. 7: A material slab of thickness t perforated with a single slit of width w surrounded by $4\times N$ grooves of width w_g and depth t_g. As $\lambda_{dB}\gg w, w_g$, the wave function inside the film is accurately described by considering only the first waveguide mode inside each indentation. If we label the indentations with index α, the wave function inside the film can be written as

$$|\Psi(z)\rangle=\sum_{\alpha=-N}^{N}\phi_\alpha(z)|\psi_{WM}^{\alpha}\rangle, \tag{20}$$

where the function $\phi_\alpha(z)$ contains the dependence on z of Ψ inside indentation α. We label the central slit with $\alpha=0$. The associated waveguide mode in real space is $\langle x|\psi_{WM}^{0}\rangle=\sqrt{2/w}\sin[\pi/w(x+w/2)]$ for $|x|<w/2$, and vanishes otherwise. As we see in Sec. III, the dependence on z is given by $\phi_0(z)=C_0e^{i\beta z}+D_0e^{-i\beta z}$, with $\beta=\sqrt{\xi k_0^2-(\pi/w)^2}$.

The waveguide mode supported by groove α ($\alpha\neq0$) has the form $\langle x|\psi_{WM}^{\alpha}\rangle=\sqrt{2/w_g}\sin[\pi/w_g(x-x_\alpha+w_g/2)]$ if $|x-x_\alpha|<w_g/2$ (where x_α is the groove position) and $\langle x|\psi_{WM}^{\alpha}\rangle=0$, otherwise. The fact that the grooves are arranged periodically allows us to write $x_\alpha=\alpha\Lambda$, where Λ is the array period. For grooves milled in the input side of the structure ($0<z\leqslant t_g$), we have $\phi_\alpha(z)=C_\alpha\sin\beta_g(z-t_g)$, whereas for grooves in the

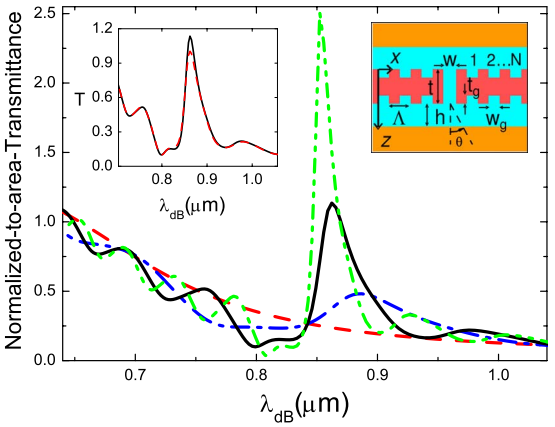

FIG. 7. (Color online) Normalized-to-area transmittance for four different structures. Dashed red line, single slit. Blue dashed-dotted line, single slit flanked by $N=5$ grooves located at each side (right and left) of the central slit at both the input and output surfaces. Black solid line and green dashed-double-dotted lines, same as before but with $N=10$ and $N=15$, respectively. Left-hand inset renders T versus λ_{dB} for $N=10$ grooves milled at the two surfaces (black solid line) or only at the input surface (red dashed line). Right-hand inset: Structure supercell containing the central slit surrounded by $4N$ grooves.

output side $(t-t_g<z\leqslant t)$, $\phi_\alpha(z)=D_\alpha \sin\beta_g(z-t+t_g)$. In both cases, the z component of the wave vector inside the grooves is $\beta_g=\sqrt{\xi k_0^2-(\pi/w_g)^2}$.

We take into account the finiteness of the structure by making the supercell length L tending to infinite $(L\to\infty)$. As a result, discrete diffraction orders cannot be defined and the matter wave function must be expanded in terms of a continuum of diffracted waves. As for periodic structures, we define the quantities ψ_α (ψ'_α), which give the amplitude of Ψ at the openings of the indentations perforated in the input (output) surface of the film. At the central slit, we have $\psi_0=C_0+D_0$ and $\psi'_0=-(C_0e^{i\beta t}+D_0e^{-i\beta t})$, whereas for $\alpha\neq 0$, $\psi_\alpha=-C_\alpha \sin(\beta_g t_g)$ and $\psi'_\alpha=-D_\alpha \sin(\beta_g t_g)$. Imposing continuity of the wave function at the interfaces of the structure, we obtain a set of $(4N+2)$ equations in the unknowns $\{\psi_\alpha,\psi'_\alpha\}$ of the form

$$(G_{\alpha\alpha}-\epsilon_\alpha)\psi_\alpha+\sum_{\gamma\neq\alpha}G_{\alpha\gamma}\psi_\gamma-G^V\psi'_0\delta_{\alpha 0}=I_\alpha,$$

$$(G_{\alpha\alpha}-\epsilon_\alpha)\psi'_\alpha+\sum_{\gamma\neq\alpha}G_{\alpha\gamma}\psi'_\gamma-G^V\psi_0\delta_{\alpha 0}=0. \qquad (21)$$

The role played by the various terms in Eqs. (21) remains the same as in Eqs. (11). The upper $(2N+1)$ equations control the flow of the matter waves at the input surface of the film, where $I_\alpha=(2\sqrt{2}i/\pi)\xi/[\xi\cos(\xi k_0 h)-i\sin(\xi k_0 h)]$ reflects the overlap between the normal incident plane wave and the waveguide mode supported by indentation α. The term ϵ_α describes the penetration of the matter waves inside the indentations. For $\alpha=0$, it has the form $\epsilon_0=\beta/[k_0\tan(\beta t)]$ whereas for $\alpha\neq 0$, $\epsilon_\alpha=\beta_g/[k_0\tan(\beta_g t_g)]$. The term $G^V=\beta/[k_0\sin(\beta t)]$ takes into account the overlap of Ψ at both sides of the film through the slit. It is only present in the equations associated to ψ_0 and ψ'_0. Finally, $G_{\alpha\gamma}=\langle\psi^\alpha_{WM}|\hat{G}|\psi^\gamma_{WM}\rangle$ describes the coupling of the matter waves coming from indentations α and γ through the SMWs traveling along the film surfaces. The representation of the propagator $\hat{G}$ in real space is

$$G(x,x')=\frac{1}{2\pi}\int_{-\infty}^{\infty}dk_x\frac{iq_z}{k_0}f(k_x,h)e^{ik_x(x-x')}, \qquad (22)$$

where the wave vector along the z direction is $k_z=\sqrt{k_0^2-k_x^2}$ in vacuum, and $q_z=\sqrt{\xi k_0^2-k_x^2}$ inside the potential well surrounding the film. The function $f(k_x,h)$ is given by

$$f(k_x,h)=\frac{k_z\cos(q_z h)-iq_z\sin(q_z h)}{q_z\cos(q_z h)-ik_z\sin(q_z h)}. \qquad (23)$$

The quantities $\{\psi_\alpha,\psi'_\alpha\}$ are found by solving Eqs. (21), and once they are known, the matter wave function in all the space can be constructed. The transmissivity of the structure is then given by the ratio between the transmitted and incident probability density current fluxes through the slit. This ratio can be expressed as a function of the matter wave amplitudes at the slit openings as $T=G^V\,\mathrm{Im}(\psi_0^*\psi'_0)$. As a difference with the preceding sections, the incident wave is now normalized to the slit width w and T corresponds to the normalized-to-area transmittance.

Figure 7 represents T versus λ_{dB} for normal incidence of the atoms. The red dashed line corresponds to the single slit case ($w=0.3$ μm and $t=0.16$ μm). As $\lambda_{dB}\gg w$, $T<1$ and the transmission spectrum shows an exponentially decaying behavior as λ_{dB} increases. When grooves ($w_g=0.22$ μm and $t_g=0.065$ μm) are milled surrounding the slit on both surfaces of the film, T develops a resonant peak close to the periodicity of the groove array $\Lambda=0.8$ μm. As the number of grooves increases from $N=5$ (blue dashed-dotted line) to $N=15$ (green dashed-double-dotted line), the transmission peak becomes higher and spectrally narrower. This is a clear fingerprint of the excitation of SMWs running along the film surfaces. For higher N, the coupling between the incident plane matter wave and the SMWs becomes more efficient, leading to a better defined resonant transmission peak. In the left-hand inset of Fig. 7, the comparison between the transmission spectrum for a single slit surrounded by $N=10$ grooves in both the input and output sides of the film (solid black line) and the same slit surrounded by $N=10$ grooves only in the input side (red dashed line) is shown. It is clear that the total transmission is mainly controlled by the corrugation placed at the input surface of the structure.

In order to study the shape of the beam emerging from the structure, we calculate the transmitted matter wave function (Ψ_t) in the vacuum region below the structure $(z>t+h$, see right-hand inset of Fig. 7). It can be written as a superposition of plane waves of the form

$$\Psi_t(x,z)=\int_{-\infty}^{\infty}dk_x t(k_x)e^{ik_z z}e^{ik_x x}, \qquad (24)$$

where the transmission coefficient $t(k_x)$ depends on the amplitudes ψ'_α as

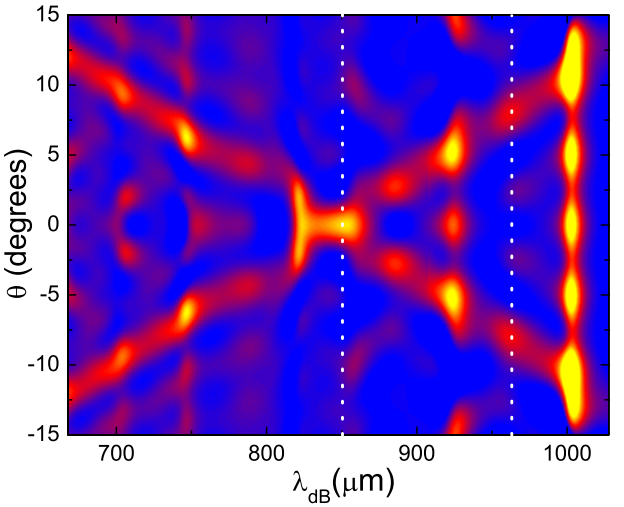

FIG. 8. (Color online) Radial probability density current j_r^t emerging from a single slit as a function of the exiting angle θ and the de Broglie wavelength λ_{dB}. The slit ($w=0.22$ μm) is flanked by $N=15$ grooves of width $w_g=0.30$ μm and depth $t_g=0.065$ μm disposed periodically ($\Lambda=0.80$ μm) at both surfaces of a film of height $t=0.16$ μm. White dashed lines indicate the λ_{dB} values considered in Fig. 9.

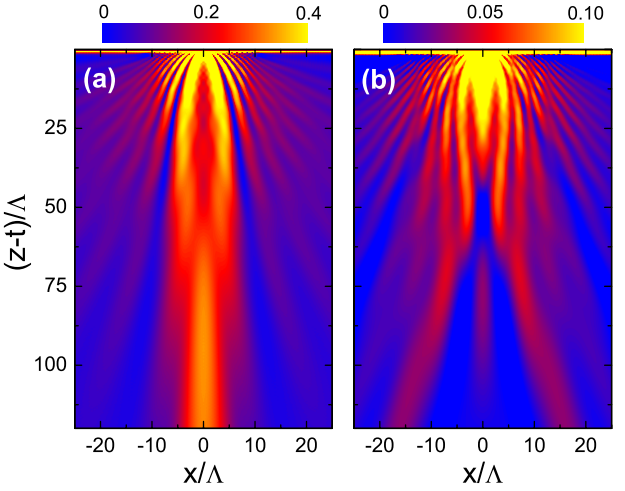

FIG. 9. (Color online) Amplitude of the matter wave function emerging from the structure considered in Fig. 8 at two different wavelengths: (a) At resonance ($\lambda_{dB}=0.85$ μm) and (b) out of resonance ($\lambda_{dB}=0.96$ μm). Note that the color scale is different in each panel.

$$t(k_x) = \frac{q_z e^{-ik_z(t+h)}}{[q_z \cos(q_z h) - ik_z \sin(q_z h)]} \times \sum_{\alpha=-N}^{N} \left(\frac{\cos(k_x w_\alpha/2) e^{-ik_x x_\alpha}}{w_\alpha [(\pi/w_\alpha)^2 - k_x^2]} \right) \psi'_\alpha. \quad (25)$$

Once Ψ_t is obtained, the radial probability density current $j_r^t=(\hbar/m)\mathrm{Im}\{\psi^* \partial_r \psi\}$ can be calculated. Figure 8 renders j_r^t in the far field ($r=150\Lambda$) as a function of the exiting angle θ and λ_{dB} for the structure with $N=15$ grooves perforated on both film surfaces. At $\lambda_{dB}=0.85$ μm, j_r^t shows a maximum around $\theta=0°$ which leads to a collimated beam emerging from the single slit in the forward direction. This λ_{dB} coincides with the position of the transmission peak in the spectrum (green dashed-double-dotted line in Fig. 7). This fact indicates that both phenomena, resonant transmission and beaming, have the same physical origin: The excitation of SMWs propagating along the film surfaces. We have also studied j_r^t for films corrugated only in the input surface. The angular patterns of j_r^t obtained display the uniform behavior characteristic of a wave emerging from a single aperture much smaller that the wavelength. From this result, we can conclude that the corrugation of the output surface of the film governs the shape of the atom beam exiting from the central slit.

Figure 9 renders the amplitude of the matter wave function emerging from a single slit flanked by $N=15$ grooves evaluated at two different de Broglie wavelengths (indicated by white dashed lines in Fig. 8). Wave function in panel (a) is associated to the peak ($T=2.5$) in transmission spectrum at $\lambda_{dB}=0.85$ μm (see Fig. 7). At resonance, the scattering of the SMWs with the grooves perforated in the output surface of the film leads to a coherent reemission of matter waves. The interference of these matter waves with those stemming from the central slit gives rise to a very collimated beam along the z direction. Panel (b) is evaluated out of resonance ($\lambda_{dB}=0.96$ μm). The transmissivity of the structure is $T=0.25$, much lower than in panel (a). As expected from Fig. 8, two different beams emerge from the structure, traveling with an angle $\theta \approx \pm 8°$. The matter wave reemission by the surface corrugation is now much less efficient than at resonance. This fact allows us to see clearly the SMWs traveling away from the central slit along the film surface.

VI. CONCLUSIONS

We have analyzed theoretically the formation of surface matter waves in vacuum-solid interfaces, with properties similar to surface plasmon polaritons. In contrast to the electromagnetic case, the Schrödinger equation requires an attractive potential surrounding the material surface in order to support such bounded solutions. By means of a simple model based on square wells, we have studied the appearance of the resonant transmission phenomenon of matter waves through periodic arrays of apertures.

We have demonstrated the appearance of the extraordinary transmission phenomenon for cold atoms in two-dimensional hole arrays. Moreover, we have shown how the scalar character of the matter wave function leads to important differences with the electromagnetic case, where polarization effects play a relevant role. We have also analyzed in detail the dependence of the phenomenon on the array geometry and hole shape.

Surface matter waves can also lead to an enhancement of matter waves transmission through a single aperture flanked by a periodic array of indentations. We have studied how a collimated beam emerging from the aperture can be obtained by tailoring the corrugation at the output side of the film.

Apart from their fundamental interest, surface matter waves constitute the bridge to transfer all phenomenology associated to surface plasmons in classical optics to the domain of atom optics. In this manner, they can help to enhance the control of neutral atoms with promising applications in fields like atom lithography [44] and interferometry [45]. Enhanced transmission and beaming phenomena have been successfully demonstrated with plasmons, photonic crystal modes, and acoustic waves. The robustness of such surface wave assisted phenomena makes us confident that careful design of the atom-surface interaction should enable the experimental verification of these effects.

ACKNOWLEDGMENTS

This work was supported by the Spanish Ministerio de Ciencia y Tecnología under Grant No. MAT2005–06608–C02, and the EU under Project No. FP6-NMP4–CT-2003–505699.

[1] T. W. Ebbesen, H. J. Lezec, H. F. Ghaemi, T. Thio, and P. A. Wolff, Nature (London) **391**, 667 (1998).
[2] E. Popov, M. Nèviere, S. Enoch, and R. Reinisch, Phys. Rev. B **62**, 16100 (2000).
[3] L. Martín-Moreno, F. J. García-Vidal, H. J. Lezec, K. M. Pellerin, T. Thio, J. B. Pendry, and T. W. Ebbesen, Phys. Rev. Lett. **86**, 1114 (2001).
[4] W. L. Barnes, W. A. Murray, J. Dintinger, E. Devaux, and T. W. Ebbesen, Phys. Rev. Lett. **92**, 107401 (2004).
[5] K. J. Klein Koerkamp, S. Enoch, F. B. Segerink, N. F. van Hulst, and L. Kuipers, Phys. Rev. Lett. **92**, 183901 (2004).
[6] J. Bravo-Abad, A. Degiron, F. Przybilla, C. Genet, F. J. García-Vidal, L. Martín-Moreno, and T. W. Ebbesen, Nat. Phys. **2**, 120 (2006).
[7] U. Schröter and D. Heitmann, Phys. Rev. B **58**, 15419 (1998).
[8] J. A. Porto, F. J. García-Vidal, and J. B. Pendry, Phys. Rev. Lett. **83**, 2845 (1999).
[9] M. M. J. Treacy, Appl. Phys. Lett. **75**, 606 (1999).
[10] Q. Cao and P. Lalanne, Phys. Rev. Lett. **88**, 057403 (2002).
[11] F. J. García-Vidal and L. Martín-Moreno, Phys. Rev. B **66**, 155412 (2002).
[12] D. C. Skigin and R. A. Depine, Phys. Rev. Lett. **95**, 217402 (2005).
[13] A. I. Fernández-Domínguez, F. J. García-Vidal, and L. Martín-Moreno, Phys. Rev. B **76**, 235430 (2007).
[14] J. Bravo-Abad, F. J. García-Vidal, and L. Martín-Moreno, Phys. Rev. Lett. **93**, 227401 (2004).
[15] F. Przybilla, C. Genet, and T. W. Ebbesen, Appl. Phys. Lett. **89**, 121115 (2006).
[16] T. Matsui, A. Agrawal, A. Nahata, and Z. Valy Vardeny, Nature (London) **446**, 517 (2007).
[17] J. Bravo-Abad, A. I. Fernández-Domínguez, F. J. García-Vidal, and L. Martín-Moreno, Phys. Rev. Lett. **99**, 203905 (2007).
[18] Y. Takakura, Phys. Rev. Lett. **86**, 5601 (2001).
[19] A. P. Hibbins, J. R. Sambles, and C. R. Lawrence, Appl. Phys. Lett. **81**, 4661 (2002).
[20] F. J. García-Vidal, H. J. Lezec, T. W. Ebbesen, and L. Martín-Moreno, Phys. Rev. Lett. **90**, 213901 (2003).
[21] H. J. Lezec, A. Degiron, E. Deveux, R. A. Linke, L. Martín-Moreno, F. J. García-Vidal, and T. W. Ebbesen, Science **297**, 820 (2002).
[22] L. Martín-Moreno, F. J. García-Vidal, H. J. Lezec, A. Degiron, and T. W. Ebbesen, Phys. Rev. Lett. **90**, 167401 (2003).
[23] H. Raether, *Surface Plasmons on Smooth and Rough Surfaces and on Gratings* (Springer, Berlin, Heidelberg, 1988).
[24] J. B. Pendry, L. Martín-Moreno, and F. J. García-Vidal, Science **305**, 847 (2004).
[25] F. J. García-Vidal, L. Martín-Moreno, and J. B. Pendry, J. Opt. A, Pure Appl. Opt. **7**, S97 (2005).
[26] E. Moreno, A. I. Fernández-Domínguez, J. Ignacio Cirac, F. J. García-Vidal, L. Martín-Moreno, Phys. Rev. Lett. **95**, 170406 (2005).
[27] A. I. Fernández-Domínguez, E. Moreno, L. Martín-Moreno, and F. J. García-Vidal, Phys. Rev. A **74**, 021601(R) (2006).
[28] M.-H. Lu, X.-K. Liu, L. Feng, J. Li, C.-P. Huang, Y.-F. Chen, Y.-Y. Zhu, S.-N. Zhu, and N.-B. Ming, Phys. Rev. Lett. **99**, 174301 (2007).
[29] B. Hou, J. Mei, M. Ke, W. Wen, Z. Liu, J. Shi, and P. Sheng, Phys. Rev. B **76**, 054303 (2007).
[30] J. Christensen, A. I. Fernández-Domínguez, F. De León-Pérez, L. Martín-Moreno, and F. J. García-Vidal, Nat. Phys. **3**, 851 (2007).
[31] U. Leonhardt, Science **312**, 1777 (2006).
[32] J. B. Pendry, D. Schurig, and D. R. Smith, Science **312**, 1780 (2006).
[33] D. Schurig, J. J. Mock, B. J. Justice, S. A. Cummer, J. B. Pendry, A. F. Starr, and D. R. Smith, Science **314**, 977 (2006).
[34] S. Zhang, D. A. Genov, C. Sun, and X. Zhang, Phys. Rev. Lett. **100**, 123002 (2008).
[35] S. A. Cummer, B.-I. Popa, D. Schurig, D. R. Smith, J. B. Pendry, M. Rahm, and A. Starr, Phys. Rev. Lett. **100**, 024301 (2008).
[36] E. G. Lima, M. Chevrollier, O. Di Lorenzo, P. C. Segundo, and M. Oriá, Phys. Rev. A **62**, 013410 (2000).
[37] J. P. Gordon and A. Ashkin, Phys. Rev. A **21**, 1606 (1980).
[38] V. I. Balykin, V. S. Letokhov, Y. B. Ovchinnikov, and A. I. Sidorov, Phys. Rev. Lett. **60**, 2137 (1988).
[39] B. H. Bransden and C. J. Joachim, *Quantum Mechanics* (Pearson Education Ltd, Essex, 2000).
[40] E. Moreno, L. Martín-Moreno, and F. J. García-Vidal, J. Opt. A, Pure Appl. Opt. **8**, S94 (2006).
[41] U. Fano, Phys. Rev. **124**, 1866 (1961).
[42] C. Genet, M. P. van Exter, and J. P. Woerdman, Opt. Commun. **225**, 331 (2003).
[43] J. Bravo-Abad, L. Martín-Moreno, F. J. García-Vidal, E. Hendry, and J. Gómez Rivas, Phys. Rev. B **76**, 241102(R) (2007).
[44] G. Timp, R. E. Behringer, D. M. Tennant, J. E. Cunningham, M. Prentiss, and K. K. Berggren, Phys. Rev. Lett. **69**, 1636 (1992).
[45] O. Carnal and J. Mlynek, Phys. Rev. Lett. **66**, 2689 (1991).